Orbiting Orbitals: Visualization of Vi-Bronic Motion at a Conical Intersection.

6 AUTHORS, INCLUDING:

Joonhee Lee
University of California, Irvine
15 PUBLICATIONS **67** CITATIONS

Karoliina Honkala
University of Jyväskylä
62 PUBLICATIONS **1,846** CITATIONS

Vartkess Ara Apkarian
University of California, Irvine
**193** PUBLICATIONS **4,093** CITATIONS

Orbiting Orbitals: Visualization of Vibronic Motion at a Conical Intersection

Joonhee Lee,[†] Shawn M. Perdue,[†] Alejandro Rodriguez Perez,[†] Patrick Z. El-Khoury,[†] Karoliina Honkala,[‡] and V. A. Apkarian[†,*]

[†]Department of Chemistry, University of California—Irvine, Irvine, California 92697-2025, United States
[‡]Department of Chemistry, Nanoscience Center, University of Jyväskylä, P.O. Box 35, FIN-40014 Jyväskylä, Finland

ABSTRACT: The Jahn−Teller (JT) active unpaired electron of single metalloporphyrin radical anions is imaged through scanning tunneling microscopy. It is demonstrated that the electron is delocalized over the porphyrin macrocycle and its topographic image is determined by vibronic motion: the orbital of the electron adiabatically follows the zero-point pseudorotation of skeletal deformations. Transformation of the polar graphs of the observed images allows visualization of the adiabatic vibrational density to which the electron is coupled. The vibronic potential at the conical intersection is visualized and the half-integer angular momentum characteristic of the Berry phase is revealed in the radial function of the electron. The measurements underscore the economy of Jahn−Teller dynamics: small atomic displacements ($\sim 10^{-1}$ Å) determined by weak interactions (~ 10 meV) control the motion of the electron on a 10 Å scale and determine the molecular shape and function.
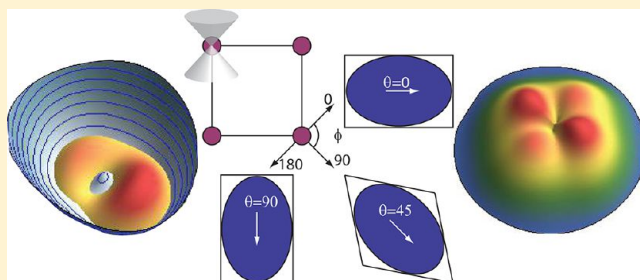
INTRODUCTION

Shapes and reactivities of molecules are determined by their frontier orbitals: the highest occupied and lowest unoccupied molecular orbitals (HOMO and LUMO). Scanning tunneling microscopy (STM) enables imaging of the shapes of molecules,[1] and under favorable conditions, MOs can be seen.[2−4] A critical requirement is to decouple the molecular electronic states from those of the conductive tip and substrate. This is commonly accomplished by using a thin dielectric barrier on which the molecule is physisorbed. At positive sample bias the unfilled LUMOs are imaged, whereas at negative bias the filled HOMOs are imaged, and a sharper definition of the MOs is attained when in addition the STM tip is terminated by a molecular adsorbate.[2,4] More commonly, the recorded topographic images are not recognizable MOs. This is generally attributed to the fact that the imaged local density of states at the Fermi surface is a strong admixture of molecular electronic states and projected surface states of tip and substrate.[5,6] Here, we recognize that even when molecules are electronically decoupled from the substrate the blurring of MOs can arise through vibronic dynamics. We illustrate this through STM imaging of the Jahn−Teller (JT) active electron on the radical anion of Zn(II) Etioporphyrin (ZnEtio⁻) adsorbed on a thin film of aluminum oxide.

ZnEtio is a representative of the family of metalloporphyrins that nature has selected for control of critical function,[7] such as light harvesting and control of electron flow in the photosynthetic reaction center.[8] Their ubiquity in biological systems has inspired extensive research aimed at understanding and emulating their function in molecular electronics.[9,10] Their electronic properties are described by Gouterman's four-orbital model:[11,12] the frontier orbitals consisting of the nearly degenerate a_{1u} and a_{2u} HOMOs and the degenerate pair of e_g LUMOs. Due to the degeneracy of orbitals and symmetry of the molecule, the excited neutral molecule and its radical ions are classic cases of JT-activity in D_{4h}-symmetry,[13,14] established through spectroscopy[15,16] and theory.[17,18] The JT theorem recognizes that in symmetric molecules, perfect electronic degeneracy is unstable: nuclear distortions that break symmetry lift degeneracy and mix orbitals.[19] The static JT limit is reached when the stabilization energy is large, in which case the molecule is permanently distorted, whereas in the dynamic limit, the orbital tracks the motion of the JT-active vibrations.[20] Now, otherwise imperceptible vibrational distortions of the molecule control its electronic shape, which should be reflected in its STM image. The corollary is a nonstandard interpretation of STM: the images have dynamic content, which if extracted can be used to visualize the underlying nuclear motion. We demonstrate this conjecture through measurements and their analysis.

We show that when ZnEtio⁻ is imaged at negative bias, its unpaired electron appears as a dumbbell aligned along one axis and delocalized over the macrocycle. Its angular momentum is quenched and the 4-fold symmetry of the molecule is reduced

to 2-fold. The state of the electron vividly illustrates the static JT limit. As the bias is scanned toward positive values, the image gradually evolves into a clover shape. We show that this shape is the signature of a rotating orbital. At the 5 K temperature of the measurements, the orbiting orbital can be understood as the dynamic JT-effect of an electron following zero-point deformations. Taking advantage of the mapping between nuclear and electronic angular coordinates generic to conical intersections[21] transforms the images to visualize the underlying adiabatic vibrational density. We "see" the avoided singularity of the cone. Moreover, from the radial profile of the apparent electron confined to a disk, we extract the fractional angular momentum dictated by the topological (Berry) phase[22] characteristic of conical intersections.[23] In effect, nuclear motion on a characteristic length scale of $\sim 10^{-1}$ Å is imaged. Neither motion nor the associated length scale is standard to the realm of STM. They appear when the electron acts as an extension of the STM tip. These considerations seem to have gone unnoticed, despite a prior demonstration of static JT-controlled topography in C_{60}[24] and associated theoretical analyses.[25] We will conclude that these considerations apply more broadly.

■ THE MEASUREMENTS

The measurements are carried out with an STM operating under ultrahigh vacuum and cryogenic conditions (4×10^{-11} Torr, $T = 5$ K). ZnEtio is sublimed on a 5 Å thick aluminum oxide layer grown on atomically flat NiAl(110), according to well established procedures.[26] The structure of the oxide, which is illustrated in Figure 1A, has been characterized previously.[27]
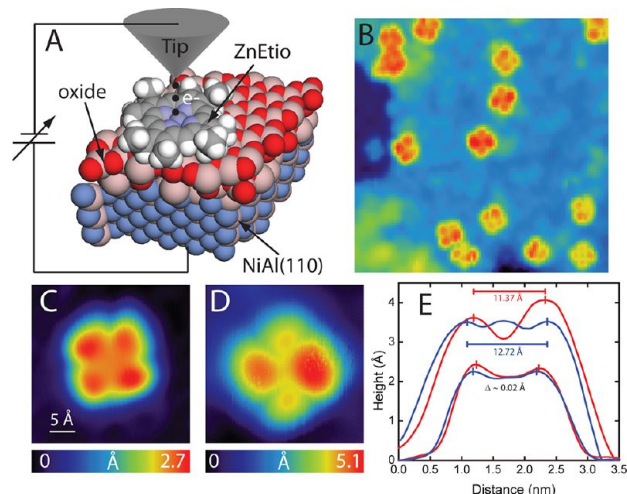

Figure 1. ZnEtio molecules on the oxide. (A) Crystal structure used in DFT calculations. (B) Variations in topography of ZnEtio on the oxide surface. On NiAl(110) the molecule has the appearance of a pinwheel (C), whereas on the oxide it is saddle-shaped (D). (E) Line profiles along cross-diagonals of molecule C (lower curves) and D (upper curves).

We use the reported lattice coordinates[28] to construct the unit cell in our DFT simulations. The oxide layer provides a second tunneling junction, which electronically isolates the physisorbed molecule from the metal substrate. In the absence of van der Waals forces the calculated adsorption enthalpy is positive by ~ 1 eV; the inclusion of van der Waals forces yields an adsorption enthalpy of -1.6 eV, using the optPBE-VdW self-consistent functional.[29] Despite the weak interaction between

molecule and substrate, the topographic images on the oxide show significant variation, as in Figure 1B. The most common occurrence is the saddle structure shown in Figure 1D, to be contrasted with the characteristic image of the molecule on the metal, Figure 1C.

On the metal, the molecule has the appearance of a pinwheel that lies flat on the surface. Its four-lobe structure preserves the 4-fold symmetry of the molecule, with chiral periphery indicating that all ethyl groups point in the same direction—away from the methyl groups to minimize steric hindrance. On the oxide, the symmetry is reduced to 2-fold, with 1 Å difference in the distance between lobes on cross-diagonals (Figure 1E). The periphery retains the chiral profile (Figure 1D), suggesting planarity: the saddle shape does not appear to be caused by out-of-plane deformation of the skeleton, as previously surmised.[30] In fact, both of these images belong to the ZnEtio$^-$ radical anion, as we show next.

ZnEtio can be reversibly charged and discharged on the oxide. This is established by the hysteretic scanning tunneling spectroscopy (STS) of differential conductance (dI/dV) versus bias voltage (V_b). The spectra of Figure 2 are recorded on the big and small lobes of the saddle (Figure 2 inset). After a large negative bias is applied, the topographic image of the molecule shows internal structure that can be associated with out-of-plane ethyl groups. As the bias is scanned, no resonances are seen until reaching the incomplete peak at 0.7 V, upon which the image changes into the saddle shape. Upon reversal of the scanning direction of the bias, two new peaks appear: the sharp resonance near 0.5 V and broad resonance near -0.5 V. The saddle shape is retained in the topographic image until crossing the -0.5 V resonance, upon which both resonances disappear and the image reverts to that of the structured initial topography. The cycle is characteristic of charging and discharging.[31] The incomplete resonance at 0.7 V is the affinity level at which the molecule is reduced. It corresponds to filling one of the E_g degenerate pair of LUMOs of the neutral, whereby the singly occupied MO (SOMO) of the radical anion moves below the Fermi level (Figure 2C). The sharp peak at 0.5 V is characteristic of Coulomb blockade, due to repulsion between tunneling electron and the negatively charged radical ion. From the sharp edge of the resonance, a lifetime of 35 fs can be inferred for the transient ZnEtio^{2-} dianion. The resonance at -0.5 V is due to current from substrate to tip that passes through the SOMO of the anion. As long as the rate of electron injection from substrate to molecule exceeds the rate of tunneling from molecule to tip, the anion remains. This steady state is overcome by lowering V_b, upon which the ion discharges and the resonances associated with it disappear. We may, unequivocally, assign the saddle shaped image to the radical anion, and the ionization resonance at -0.5 eV to the unpaired electron. Because the SOMO of the ion is below the Fermi level of NiAl, the molecule will be spontaneously charged on the metal—the pinwheel topography belongs to ZnEtio$^-$ on the metal.

Remarkably, although all aspects of the cyclic STS are reproduced, the ionization resonance is absent on the small lobes. The molecule can be charged, and upon charging the Coulomb blockade is observed; however, the ion does not discharge when the tip is placed on the small lobe. As the bias voltage is scanned from positive to negative values, the saddle structure gradually evolves into the dumbbell (see images 4, 5, and 6 in Figure 2B). At $V_b < -0.5$ V the unpaired electron is confined to the big lobes, and that defines the discharge map
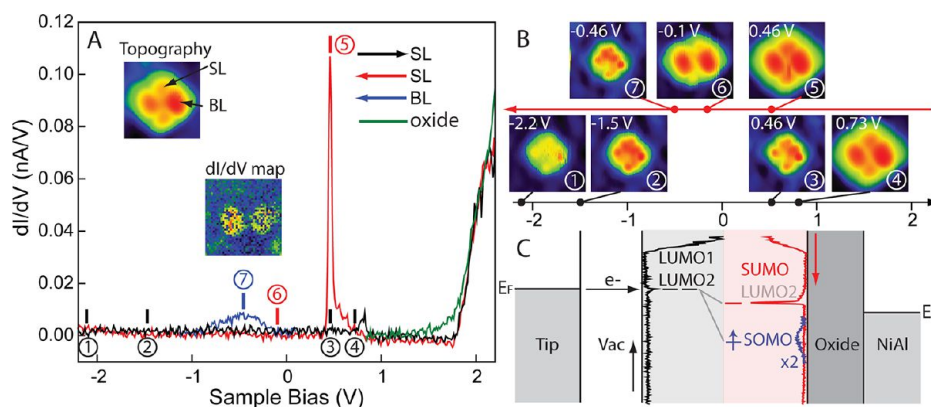
Figure 2. (A) dI/dV spectra of a single ZnEtio. The black/red curves and the blue curve were recorded on the small lobe (SL) and big lobe (BL), respectively. The arrows indicate the scanning direction of the bias. The blue peak appears only on BL. The dI/dV map at ~−0.5 V shows that the signal is localized to the BLs. (B) Hysteretic topography at bias points marked in (A). (C) Energy diagram showing the lifting of orbital degeneracy by single electron charging. The dI/dV map in (A) is recognized as the unpaired electron with quenched angular momentum.

shown in the inset of Figure 2A. Locked onto the equatorial (x-)axis of the molecule, the image is recognizable as the density, ψ^2, of the π_x state of an electron confined to the porphyrin disk. Its angular momentum is quenched and the orbital is permanently locked onto the lattice. The reduced symmetry of the electron (D_{2h}) and the quenching of its angular momentum can be regarded as direct manifestations of the static JT effect.

The alignment of the electron orbital relative to the lattice of the oxide is illustrated in Figure 3. The resolved unit cell is a parallelogram, with dimensions (9.3 Å × 19.4 Å) close to LEED results (10.55 Å × 17.88 Å).[32] The angle between the short side of the parallelogram and the [001] direction is 38°, larger than

a prior report of 24°, although similar distortions were seen in the same work.[33] This deviation is attributed to the strain induced by the incommensurate structures of oxide and NiAl, and the relatively small size of the oxide under investigation (~200 Å × 200 Å). The referenced prior is for a fully covered oxide surface.[33] Given the complexity of the unit cell, it is difficult to precisely determine the adsorption site. The same applies to our DFT calculations. However, alignment of the orbital lobes relative to the cell can be tracked experimentally. The two images shown in Figure 3C,D are for the same molecule, before and after being tossed by 11 Å. The translation is accompanied by a discrete 45° rotation of the image, while retaining its saddle shape. Although the alignment of lobes is locked by crystal fields, the observed rotation angle does not correspond to any symmetry direction on the lattice. Both the saddle shape and the discrete rotation angle are inherent to the molecular Hamiltonian. In all, nine saddle-shaped molecules were investigated at length. All nine show the hysteretic STS, and have in common the main observations reported above.

INADEQUACY OF BO ORBITALS

The unpaired electron of the isolated ion occupies one of the doubly degenerate E_g states shown in Figure 4B,C. In D_{4h} symmetry, they mix through in-plane, rectangular, and rhombic vibrations that transform according to b_{1g} and b_{2g} irreducible representations, respectively. There are nine normal modes of each symmetry in the porphine frame—all nine couple to different degrees to affect the overall distortion that globally lowers the state energy.[34] We show in Figure 4E,F calculated orbitals of the anion. When the molecular frame deforms along the rectangular (b_{1g}) minimum, recognized by the 0.04 Å elongation of the equatorial N−N distance in Figure 4D, the orbital locks on E_{gx} with density localized along the equatorial axis and depleted along the poles (on β-carbons of the pyrroles along the y-axis). An accurate treatment of the degenerate system would require multiconfiguration methods.[35]

The DFT results presented here are meant to serve as a reference. First, we highlight the scales involved: Small displacements in atomic positions (~0.04 Å), driven by small stabilization energies (~20 meV), control electronic structure over the ~10 Å diameter of the molecule. Only the latter scale is observable in STM. Second, we note that although the JT effect is vividly captured by the recorded image of the unpaired
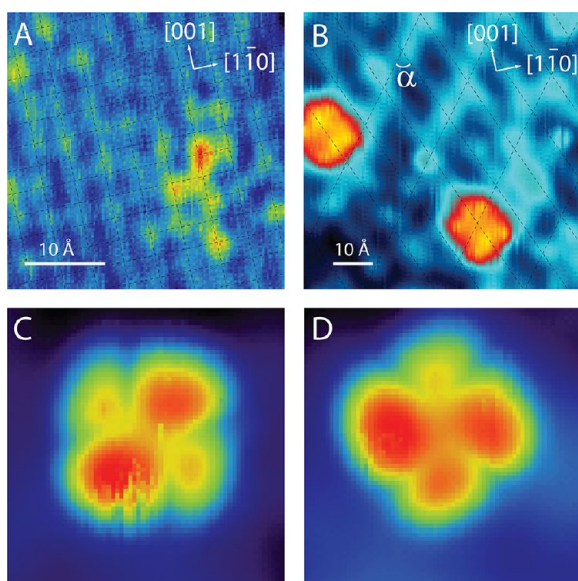

Figure 3. Interaction between ZnEtio⁻ and substrate. (A) Atomically resolved NiAl(110) surface. Aluminum atom rows are regularly spaced with troughs along [110], whereas atoms on rows along [001] are not well resolved due to very small variation in the density of states along that direction. The unit cell is 2.89 Å × 4.08 Å. (B) ZnEtio⁻ and the oxide lattice are simultaneously resolved at 20 pA, +0.5 V. NiAl(110) crystallographic directions are overlaid with lines to guide the eye. The unit cell is a parallelogram: 19.4 Å × 9.3 Å with corner angle α = 61°. (C, D) ZnEtio⁻ before and after toss by 11 Å, the translation is accompanied by a 45° rotation of the image.
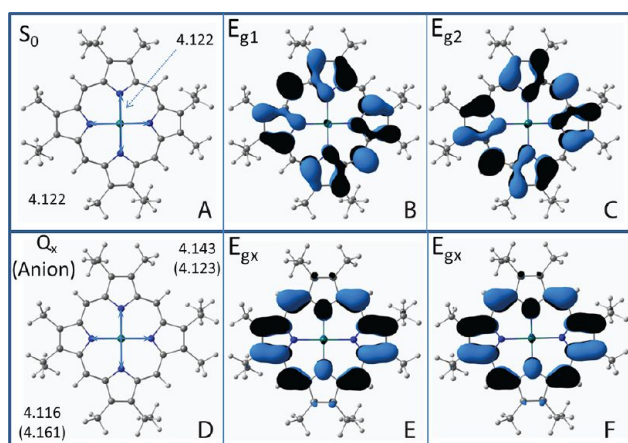
Figure 4. (A) Fully optimized structure of ZnEtio in its ground electronic state, and its degenerate LUMOs (B, C). (D) Displaced N−N distances in the fully optimized structure of the singly charged ZnEtio, which locks the orbital into E_{gx} (E). The E_{gy} orbital is shown in (F). Calculations were performed using the B3LYP/def-SVP and UB3LYP/def-SVP levels for the neutral molecule and anion, respectively.

electron (dI/dV map in Figure 1A), the observed density bears no resemblance to the calculated E_{gx} orbital (Figure 4E). For well-isolated states, STS images should map out the MO density as established through applications of the Tersoff−Hamann formalism.[5] Because in the present the single E_g orbital is involved, in a strict BO picture the same image would be expected at all biases: the half-filled orbital at positive bias and the half-empty orbital at negative bias. Yet, it is difficult to see the connection between the observed π_x-orbital of the SOMO (at −0.5 V), or pinwheel and saddle-shaped SUMO, and the rich nodal structure of the MOs seen in Figure 4. The discrepancy cannot be attributed to experimental resolution either, because finer substructure is seen in the topography of the neutral molecule. Finally, we note the apparent delocalization of the unpaired electron evidenced by the reversible flipping of the ethyl groups into and out of the molecular plane upon charging and discharging, respectively (images 3 and 4 of Figure 2B). In the calculated structures of both neutral and ion the ethyl groups remain out-of-plane due to hyperconjugation.[36] Therefore, the planarity imposed on the molecule upon charging suggests that the unpaired electron is delocalized over the entire macrocycle, stabilized by maximizing the size of the disk on which it is confined.

■ VIBRONIC ANALYSIS

The topographic images can be understood in terms of a JT-active electron confined to the porphyrin disk. The essential considerations, which we give explicitly, are summarized in Figure 5. We start by considering the vibronic Hamiltonian:

$$H = H_e + H_{ev} + H_v \tag{1}$$

in which H_{ev} describes the coupling between electronic and vibrational degrees of freedom. Ignoring spin−orbit coupling, which is small for π-electrons,[37] the consideration is limited to the degenerate pair of E_g eigenstates of H_e. They can be represented in polar coordinates:

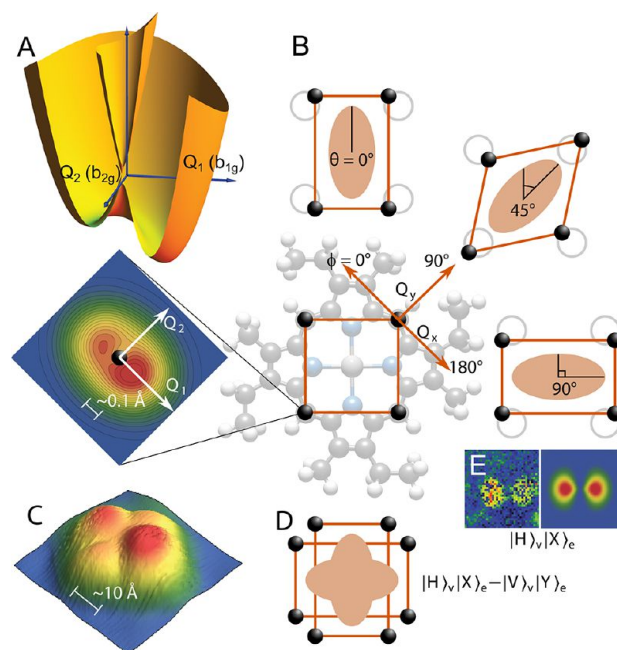$$|\pm\rangle = E_x \pm iE_y = \psi_e(r) \exp(\pm i\vartheta) \tag{2}$$

Figure 5. Jahn−Teller construct. (A) Potential energy surfaces at the conical intersection. The contour plot beneath, which appears as the 2D projection of the lower surface, is the vibrational density extracted from the experimental (C) topography. (B) The 2D deformation of the square along orthogonal b_{1g}(rectangle) and b_{2g}(diamond) coordinates generates the pseudorotation of the vertices along angle φ. The deformation drags the orbital (inscribed ellipse) along angle ϑ. φ rotates by 180°, whereas ϑ rotates by 90°. (D) The entangled coherent superposition of orbital and deformation occurs when the wave function is delocalized in the two wells of the lower potential and leads to the experimentally observed density (C). (E) When the deformation is locked on the horizontal rectangle $|H\rangle_v$, the orbital is locked onto the $|X\rangle_e$ state, as shown by the experimental image and its simulation. This static JT limit is reached at a bias of −0.5 V, due to the crystal field strain of the polarized oxide film.

associating a unit angular momentum, $\Lambda = \pm 1$, with their rotation in the 2D state space. The functional form of H_{ev} can be deduced by the requisite matrix elements to mix the two states, $\langle \mp | e^{\mp i2\vartheta} | \pm \rangle = \langle \mp | \cos(2\vartheta) \mp i \sin(2\vartheta) | \pm \rangle$.[38,39] Noting that $\cos(2\vartheta)$ and $\sin(2\vartheta)$ transform according to the irreducible $b_{1g}(x^2 - y^2)$ and $b_{2g}(xy)$ representations in D_{4h}, to lowest order, the JT-active deformation can be defined and represented in polar coordinates:

$$
\begin{aligned}
\langle \mp | H_{ev} | \pm \rangle &= \sum_{j \in b_{1g}} c_j Q_j \pm i \sum_{j \in b_{2g}} c_j Q_j \\
&= c_1 Q_1 \pm i c_2 Q_2 \\
&= Q \exp(\pm i\varphi)
\end{aligned}
\tag{3}
$$

Here, the angle brackets imply integration over electronic degrees of freedom. φ defines the pseudorotation angle that connects the rectangular (b_{1g}) and rhombic (b_{2g}) distortions illustrated in Figure 5. The adiabatic motion can be inferred from the construction in Figure 5: as the deformation rotates by an angle $\varphi = 0 \rightarrow 2\pi$, the orbital rotates by an angle $\vartheta = 0 \rightarrow \pi$. This seemingly simple observation leads to the profound consequences first recognized by Longuet-Higgins.[20] The required 4π rotation in φ for the vibronic wave function to return on itself implies that it is double valued, $\psi(\varphi + 2\pi) = -\psi(\varphi)$, and its angular momentum has fractional quantum

numbers, $l = m + 1/2$, where $m = 0, 1, 2, \ldots$ is the projection of pseudorotation momentum on the quantization axis shared by electron and deformation. The coupling leads to the geometric (Berry) phase[22] generic to dynamics at conical intersections.[21] The conical surface that splits the electronic degeneracy is obtained by diagonalizing H_{ev}, which in the real electronic basis, $|X\rangle = (|+\rangle + |-\rangle)/2$ and $|Y\rangle = i(|+\rangle - |-\rangle)/2$, and scaled coordinates, $c_1 Q_1 = Q_x$, $c_2 Q_2 = Q_y$, takes the simple form

$$H_{ev} = c_1 Q_1 \sigma_z + c_2 Q_2 \sigma_x = \begin{bmatrix} Q_x & Q_y \\ Q_y & -Q_x \end{bmatrix} \quad (4)$$

The eigenvalues define the double cone, $V_{ev} = \pm Q$, with associated eigenfunctions:

$$\psi_- = \sin(\varphi/2)|X\rangle - \cos(\varphi/2)|Y\rangle = \psi_e(r) \sin\left(\frac{\varphi}{2} - \vartheta\right) \quad (5a)$$

$$\psi_+ = \cos(\varphi/2)|X\rangle + \sin(\varphi/2)|Y\rangle = \psi_e(r) \cos\left(\frac{\varphi}{2} - \vartheta\right) \quad (5b)$$

And the eigenvectors, $[v_x, v_y]$, define the orbital orientation $\vartheta = \tan^{-1}(v_y/v_x)$:

$$\vartheta_+ = \varphi/2 \qquad \vartheta_- = (\varphi + \pi)/2 \quad (6)$$

This 2:1 relation between angles spanned by the orbital and the deformation, which is apparent in the construction of Figure 5, holds rigorously in (Q_x, Q_y). In these scaled coordinates the cone appears symmetric (circular), rendering the present $E \otimes (b_1 \oplus b_2)$ problem indistinguishable from that of $E \otimes e$ where the vibrations are doubly degenerate.[14] Because b_1 and b_2 modes are independent, the cone is generally elliptic in the (Q_1, Q_2) coordinates defined in (3). For a given ellipticity $\beta = c_1/c_2$, the angular relation becomes:

$$\vartheta_\pm = \tan^{-1}\left(\frac{\sin\varphi}{\beta\cos\varphi \pm \sqrt{\beta^2 \cos^2\varphi + \sin^2\varphi}}\right) \quad (7)$$

which reduces to (6) for $\beta = 1$. Independent of the choice of coordinates, the definite relation between orbital orientation ϑ and deformation angle φ implies a 1:1 map between their angular distributions. Equivalently, the observable angular distribution of the orbital, $\rho_e(\vartheta)$, determines the pseudorotation angle density $\rho_v(\varphi)$ of the hidden deformation, and vice versa. On a symmetric cone, because $\rho_v(\varphi)$ is isotropic for arbitrary energy $E = Q_0$, so is $\rho_e(\vartheta)$. On an elliptic cone, in addition, there will be an anisotropic contribution given by the asymmetry in H_{ev}.

For $c_1 > c_2$:

$$\rho(\vartheta, \varphi; Q_0) = \rho_0 + (1 - \beta^{-1})|X,Y\rangle Q_x \sigma_z \langle X,Y|$$

$$= \rho_0 + (1 - \beta^{-1}) Q_0 \cos\varphi \cos 2\vartheta \quad (8a)$$

For $c_2 > c_1$:

$$\rho(\vartheta, \varphi; Q_0) = \rho_0 + (1 - \beta)|X,Y\rangle Q_y \sigma_x \langle X,Y|$$

$$= \rho_0 + (1 - \beta) Q_0 \sin\varphi \sin 2\vartheta \quad (8b)$$

The anisotropy in the hidden vibrational distribution is bimodal (peaked at $\varphi = 0, \pi$ for $c_1 > c_2$ and at $\varphi = \pm\pi/2$ for $c_2 > c_1$), but

the anisotropy in the observable electron density is quadrupolar ($\cos 2\vartheta/\sin 2\vartheta$), aligned along the mode with the larger coupling. We recognize that the common four-lobe motif observed in the topography of the radical ion is characteristic to the $E \otimes (b_1 \oplus b_2)$ Hamiltonian. Also, the 45° rotation associated with the switching of preferred axes in (8) provides a unique explanation for discrete 45° rotations seen among molecules on the oxide (Figure 3C,D). More generally, we recognize that the $\{0 \to \pi\}$ interval of the polar graph of the observable electron density, $\rho_e(\vartheta)$, maps out the complete $\{0 \to 2\pi\}$ distribution of the vibrational deformation, $\rho_v(\varphi)$. The latter is more directly interpretable, because in addition to the cone structure, the vibronic density is determined by the vibrational distribution (Q_0) sustained on the full vibronic potential.

The $\vartheta \to 2\vartheta = \varphi$ transformation of the polar graphs of pinwheel and saddle are shown in Figure 6A,B. They reveal

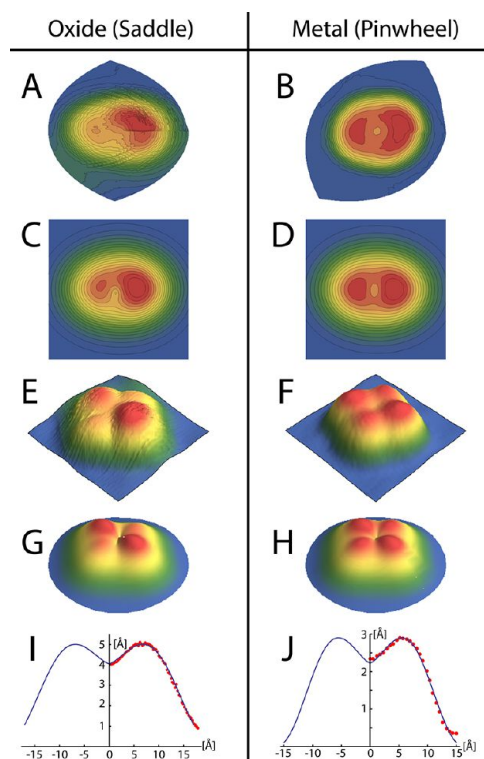**Figure 6.** Visualization of the adiabatic vibrational density at the conical intersection: (A, B) $\theta \to 2\theta = \phi$ map of the topographic images; (C, D) calculated vibrational densities. The image on the metal shows the hole due to the avoided singularity at the origin. (E, F) Experimental topographic images and their reproduction (G, H) based on the calculated vibrational densities. (I, J) The radial profile of the experimental electron density (red points) fits to $\rho(r) = (aJ_0 + bJ_{3/2})^2$ and identifies the characteristic half-integer angular momentum ($l = 3/2$).

textbook images of the adiabatic vibrational density sustained at the $E \otimes (b_1 \oplus b_2)$ vibronic potential.[14,17,40] On the metal, we see the double-well structure and the pseudorotation density that connects the wells by circumventing the singularity at the origin. Although distorted, the same features are evident on the oxide. To account for site- and bias-dependent topographies, in addition to the molecular Hamiltonian, it is necessary to include coupling between molecule and substrate. To this end, we adopt the minimally parametrized form of the vibronic

E

dx.doi.org/10.1021/jp311894n | J. Phys. Chem. A XXXX, XXX, XXX–XXX

potential, which has been previously used to explore JT-dynamics of porphyrins:[17]

$$V_\pm(Q;\varphi) = V_v + V_{ev}$$
$$= \frac{1}{2}(k_1 Q_1{}^2 + k_2 Q_2{}^2)$$
$$\pm \sqrt{(c_1 Q_1 + \delta_1)^2 + (c_2 Q_2 + \delta_2)^2} \qquad (9)$$

in which $\delta_{1,2}$ represent the crystal field strains projected along $b_{1g,2g}$ coordinates. We only need to consider zero-point motion on the lower surface to understand the content of topographic images recorded at $T = 5$ K. In Figure 6C,D we show surfaces generated according to (9) that closely match the transformed experimental densities (Figure 6A,B). We evaluate the vibrational densities sustained on these surfaces classically, $\rho_v(Q,\varphi) = \exp(-V_-(Q,\varphi)/E_0)$, in which E_0 plays the role of zero-point energy; and we recover the topographic images shown in Figure 6G,H by doubling the angle in the argument of the vibrational density: $\rho_\varepsilon(r,\vartheta) \sim \rho_v(Q,2\varphi)$.[41] The general agreement between experiment and simulation obtained with the $\varphi = 2\vartheta$ mapping (6) is due to small ellipticity: in all cases we find $0.9 < \beta < 1.2$ (Table 1). We highlight the essential features of the observed topographies within the previously catalogued parameter space of (9):

(a) For $\delta_1 = \delta_2 \sim 0$, the surface sustains four extrema: $Q_i{}^* = \pm c_i/k_i$ with associated JT stabilization energies $E_{JTi} = c_i^2/2k_i$. In the special case where $E_{JT1} = E_{JT2}$, the surface is an elliptic Mexican hat with ellipticity given by $c_1 k_2/c_2 k_1$. Otherwise (if $E_{JT1} > E_{JT2}$), the surface has two symmetric minima (at $\varphi = 0$ and π) and two saddle points (at $\varphi = \pm \pi/2$). This is approximated by the vibrational density on the metal, Figure 6B. We see the two wells connected by the density that tunnels under the saddles and depleted density at the origin. The wells are unequal in depth ($\delta_1 > \delta_2 \sim 0$) and the image has ellipticity $c_1 k_2/c_2 k_1 \sim 1.1$.

(b) For $E_{JT} \geq \delta_{1,2} \neq 0$, the cone is tilted, the intersection is eccentric, and the two well depths are unequal. This describes the vibrational density on the oxide, Figure 6A. By referencing to the topography of the neutral, it is possible to establish that the minima are along the rectangular (b_1) distortion ($c_1 > c_2$). The two wells correspond to horizontal $|H\rangle_v$ and vertical $|V\rangle_v$ rectangles; as such, the quadrupolar dimple can be associated with the entangled vibronic superposition, $|H\rangle_v|X\rangle_e - |V\rangle_v|Y\rangle_e$ depicted in Figure 5.

(c) For $\delta > E_0$, where the difference in well depths is larger than zero-point energy, the ground state is localized in one well. As long as $E_0 > k_B T$, the molecule is permanently deformed and the strict static JT limit is attained. This is the case for the discharge map shown in Figure 5E. Because now $\langle \varphi \rangle = 0$ is sharply defined, the observable electron density is that of the base function (5a): $|\psi_-|^2 = \psi_e^2(r) \sin^2 \vartheta$, whereby its radial function can be extracted (see below).

(d) For $\delta_1 \neq \delta_2 > E_{JT}$, the surface is tilted and sustains a broad minimum along the tilt of the plane. When this prevails, JT-dynamics becomes secondary: the electron is strongly coupled to the substrate and controlled by the local lattice potential and its symmetries. Topographic images that show odd symmetry, examples of which can be seen in Figure 1, necessarily belong to this limit.

The parameters that yield the simulated pinwheel and saddle are collected in Table 1. All values are scaled to the zero-point

Table 1. Parameters Used in Eqs 9 and 10 of the Text To Reproduce Observed Images (All Energies Scaled to Zero-Point, E_0)

	pinwheel		saddle	
	$\lambda = 0$	$\lambda \neq 0$	$\lambda = 0$	$\lambda \neq 0$
k_1/k_2	1.04	1.08	1.07	1.09
c_1/c_2	1.15	1.12	1.20	1.17
E_{JT1}/E_{JT2}	1.37	1.36	1.54	1.48
δ_1/E_0	0.12	0.14	0.18	0.27
δ_2/E_0	0.03	0.05	0	0
E_{JT1}/E_0	0.38	0.98	1.58	1.98
E_{JT2}/E_0	0.27	0.72	1.03	1.34
λ/E_0	0	1.42	0	1.00

energy, E_0. We note that neither the transformed images (Figure 6A,B) nor their forward simulations (Figure 6C,D) associate a length scale with the map of the vibronic density or potential. However, on the basis of low-frequency JT active modes, $(\hbar/\mu\omega)^{1/2} \sim 10^{-1}$ Å, can be associated with the full scale of these images. Consistent with recent analysis,[34] stabilization energies are small, comparable to zero-point energies; therefore, the associated deformations are within zero-point amplitudes of motion.

The apparently faithful mapping between electronic and nuclear densities, $\rho_\varepsilon(r,\vartheta)$ and $\rho_v(Q,\varphi)$, seen in Figure 6 can be traced to the nature of the electronic state. In general, there is not a direct connection between the radial functions, which are solutions of separate H_e and H_v Hamiltonians—only angles and angular momentum are shared between the two motions. Here, r and ϑ are intimately connected. For an electron delocalized over the porphyrin plane, the wave function is that of a particle confined to a disk:

$$\psi_e(r,\vartheta) = J_l(ar) \exp(\pm il\vartheta)$$

in which $J(\alpha r)$ is the cylindrical Bessel function with first root determined by the radius of the disk. As such, the angular and radial parts of ψ_e are associated through the angular momentum l. The radial function of the electron extracted from the discharge image, when the orbital is locked on one well, yields $\rho_e(r,\vartheta) = \psi_e^2(r) \sin^2 \vartheta = J_{1/2}^2(\alpha r) \sin^2 \vartheta$ and identifies the characteristic fractional angular momentum, $m = 0$, $l = 1/2$, as shown in Figure 5E. In the pinwheel and saddle topographies, where the orbital acquires pseudorotation momentum, the radial profiles perfectly fit the sum of two terms, $\rho(r) = (aJ_0 + bJ_{3/2})^2$, as shown in Figure 6I,J. Motion is hidden in the J_0 term, which reflects the isotropic part of the vibronic density, ρ_0 in (8). Motion of the orbital is evident in the anisotropy, which identifies the correct fractional angular momentum, $l = 3/2$. Thus, in addition to the characteristic angular distributions (8), the observed radial profiles independently identify the governing physics.

Deviations from the assumed D_{4h} symmetry are clearly evident and anticipated. The ethyl groups already break this symmetry in the molecule and lead to chirality associated with its pinwheel appearance. This is more clearly seen in the marginals of the 2D topographic distributions, $\rho(\vartheta) = \int \rho(r,\vartheta) dr$, which are rigorously transferrable between electronic and nuclear functions. Chirality is contained in the sawtooth distortion of the graphs presented in Figure 7. A trivial
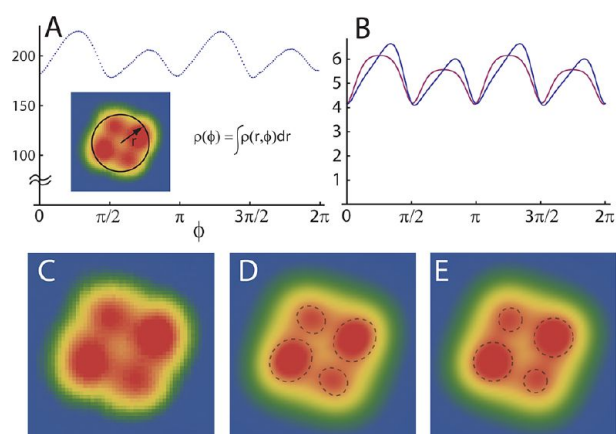
Figure 7. Chirality. (A) Radially integrated topography. (B) Simulated angular distribution of electronic density with (blue) and without (purple) inclusion of vibrational coupling $c_3 Q_1 Q_2$ in (10). (C) Experimental topography of a ZnEtio$^-$ on NiAl(110). (D, E) Simulated topography, with and without vibrational coupling. Dashed encircling lines are to aid in the recognition that the chirality arises from the tilt of the lobes due to mode coupling.

interpretation is that the electron is delocalized over a disk with modulated periphery. The vibronic reconstruction of these graphs is more naturally obtained by the inclusion of coupling between b_1 and b_2 vibrations. Adding a bilinear coupling $c_3 Q_1 Q_2$ to (9), and after minor adjustment of parameters, the radially integrated nuclear density $\rho(2\varphi) = \int \rho(Q, 2\varphi) \, dQ$ can be brought into agreement with the observable marginal (Figure 7B). The vibronic interpretation suggests that skeletal modes, which are no longer strictly orthogonal, are involved in (3). This is consistent with a recent analysis of polarized luminescence in Pt-porphyrins.[42] The inclusion of the bilinear coupling also reproduces the apparent tilt of lobes in the topographic images (Figure 7). In effect, a detailed reproduction of the observed topographies provides a physically meaningful dissection of the vibronic Hamiltonian.

Understanding the effects of bias and substrate on the observed shapes of the molecule is of interest. The bias leads to the gradual evolution of the four-lobe structure into two lobes as it is reduced to the point when the molecule discharges. This effect is entirely reproduced by increasing the crystal field strain, δ_1 in (9), as shown by the sequence in Figure 8. In effect, the potential well along the horizontal rectangle becomes gradually deeper than that along the vertical rectangle (Figure 5). Physically, biasing leads to polarization of the oxide layer by the potential drop, $\Delta V \sim 0.1 V_b$, across its thickness. We would expect a strong coupling to the electron by the excess charge
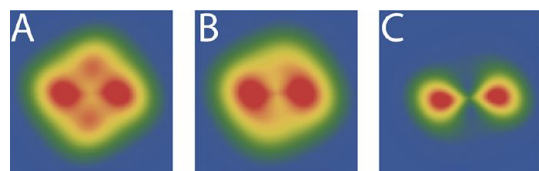

Figure 8. Simulated bias dependence of topography. The evolution seen in Figure 2 is reproduced by adjusting the single crystal field parameter, δ_1 in eq 9: (A) $\delta_1/E_0 = 0.27$ for image recorded at +0.73 V; (B) $\delta_1/E_0 = 0.46$ for image at −0.1 V; (C) $\delta_1/E_0 = 2$ and $\lambda = 0$ for the dI/dV map of the SOMO at −0.4 V, in which the orbital angular momentum is quenched.

that accumulates under the molecule. However, microscopic details of the process, explored through DFT calculations, remain a challenge at present. For an illustrative example of the reorganization energies of an insulating film associated with the charging of an adsorbate, we refer to investigations of the multiple charge states of Ag atoms on NaCl, which affords a detailed analysis.[43]

In the same manner, although we do not have a detailed assignment of adsorption sites and structures, the diversity in the molecular shapes seen on the oxide can be rationalized. When JT stabilization energies along two active deformation coordinates are similar (Table 1), small perturbations dictate shape. The perturbations may be internal or substrate induced. Thus, when $c_1 \sim c_2$, nonlinear JT-coupling and tilting of the cone via internal or external coupling become important. Restricting the description of coupling to the substrate to phenomenological strains, we recognize that they need not be limited to the two terms assumed in (9), rather the strains should be projected along the local symmetries of the oxide and possibly of the underlying metal. Thus, with physically justifiable additional parametrization of (9), while keeping to first-order JT coupling:

$$V_{ev} = s_x x + s_y y \pm \left[(c_1 Q_1 + \delta_1)^2 + (c_2 Q_2 + \delta_2)^2 + \lambda^2 \right]^{1/2}$$

(10a)

$$V_v = \frac{1}{2}(k_1 Q_1{}^2 + k_2 Q_2{}^2) + c_3 Q_1 Q_2$$

(10b)

in which $s_{x,y}$ describes the tilt of the cone along lattice coordinates, and λ maybe associated with spin−orbit coupling, which may not be negligible for the delocalized electron, or simply as strain along the coupled vibrations. The observed diversity in topography can be reproduced through (10). We give representative examples in Figure 9 in which we follow the reversible contortions in the image of one molecule during extended exposure to tunneling current at high bias. The molecule starts as a saddle aligned to the lattice. It undergoes a 45° rotation during the manipulations, which we understand to be due to switching of the preferred coupling axis (b_1/b_2) according to (8a,b). In the final frame it approximates a pinwheel; therefore, lattice strains become nearly isotropic. During the course we see the breaking of the even symmetry of the molecule (Figure 9C) due to strains along the lattice rather than internal coordinates of the molecule. Also, we see the extreme case of localizing the vibronic Hamiltonian in one well, at V_b = 3.4 V (Figure 9E). Clearly, the diversity in shape, or induced variations in the shape of one molecule, must be driven by variations in the structure and charging of the oxide layer beneath the molecule. The electron image may be used to categorize structural variations in the oxide. The principle conclusion to transmit here is that: small perturbations to the vibronic Hamiltonian of the JT-active electron generate observable changes in the shape of the molecule.

■ CONCLUSIONS

Although we do not have a firm basis to rationalize the apparent delocalization of the unpaired electron on ZnEtio$^-$, it admits a simple solution of the electronic states as those of a particle confined to a disk. The JT-dynamics then reduces to a model problem of an electron coupled to distortions of the disk, very similar to the original model of the dynamic JT effect treated by Longuet−Higgins.[20] The extensive literature on the subject is concerned with determining level structures
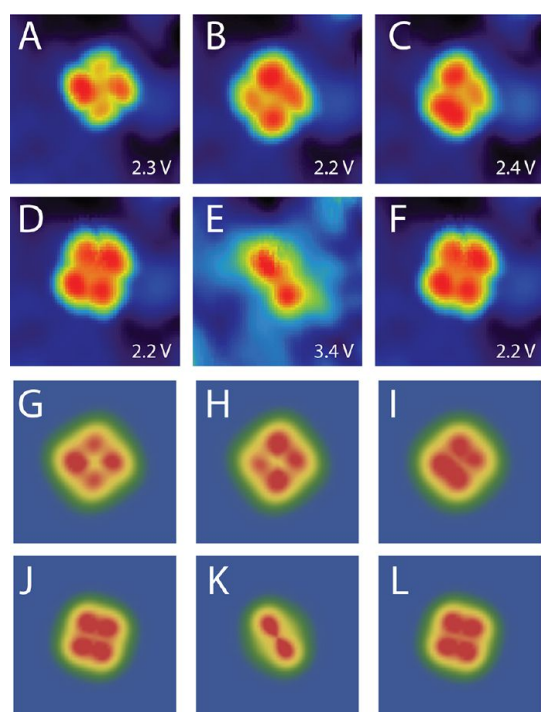
Figure 9. Variations in shape of one molecule (A−F) induced by applying high voltage (>2.4 V) in the course of scanning. The observed shapes can be reproduced (G−L) by introducing tilting of the cone along lattice coordinates, $s_x x + s_y y$, in eq 10.

(eigenvalues) that arise as a consequence, which can be observed in spectroscopic measurements.[14] Rather than eigenvalues, here the eigenfunctions become observable. We visualize the process through the observable electron density and the adiabatic vibrational density to which it is slaved. The vibronic potential characteristic to the $E \otimes (b_1 \oplus b_2)$ conical intersection in D_{4h} symmetry is directly revealed and the fractional angular momentum generic to the Berry phase is apparent in the radial function of the electron. The ubiquity of conical intersections in molecular systems and the critical role they play in determining photophysics and chemistry has been nicely reviewed.[23] They appear in diverse fields in materials science and in physics, most popularly exemplified by the Bohm−Aharonov effect.[44,45] It would seem that the present is the first direct visualization of the intersection, which is otherwise only recognized by its consequences.

Perhaps it is not too surprising that the shape of a JT-active molecule is determined by its vibronic Hamiltonian and that this is reflected in its STM image. Clearly, where vibronic coupling prevails, images cannot be rationalized in Born−Oppenheimer constructs. The consideration does not appear to be limited to molecules of known JT or pseudo-JT activity. Depending on the alignment of MOs with the Fermi level of the underlying substrate, charge transfer can lead to vibronic activity. This was illustrated by the case of ZnEtio on bare NiAl, where it is reductively adsorbed. Beyond this obvious consideration, vibronics can be expected to be more pervasive in STM measurements than appreciated. Past perturbative approaches,[5] the sum over interfering elastic scattering channels contained in the ESQC method finds broad applicability in the interpretation of STM images.[6] It is not obvious that vibronic scattering channels, which appear in electron tunneling spectroscopy,[46] can be ignored in such calculations. In effect,

we demonstrate that vibronic states dramatically influence observable shapes and are sensitive to bias- and site-dependent perturbations on what may be regarded as a weakly interacting substrate. To the extent that electronic shape dictates reactivity and function, e.g., directional conductivity[47] and current switching[48] accessible on single porphyrins, the observed diversity in shapes illustrates the efficacy of function control in JT active molecules. This sensitivity can be surmised as key to the JT economy that nature takes advantage of—small variations in molecular strain control its function.

The framework we provide for the interpretation of images should be possible to adapt in the analysis of related systems. In many reported images from a large literature on STM studies of single porphyrin molecules,[30,31,49,50] the dynamical information content can be readily inferred. For example, MgP$^+$ appears elliptic on gold,[50] which implies that the vibronic potential approximates the Mexican hat ($c_1 \sim c_2$, $\delta_{1,2} \sim 0$, $Q_1 \neq Q_2$). On NaCl, it is bistable, its image switches between $\rho(r) \cos^2 2\theta$ and $\rho(r) \sin^2 2\theta$ structures.[50] Rather than rigid body rotation, our analysis suggests that the electron switches between b_{1g} and b_{2g} deformations. The same vibronic switching dynamics occurs in ZnEtio$^-$, as we report elsewhere. In the case of MgP$^+$, the potential must sustain four wells, which occurs in quadratic coupling, when $c_1 \sim c_2$. Indeed, the bistability disappears when the molecule exhibits eight lobes,[50] which occurs when the quadratic minima are not distorted by the lattice. Clearly the simple angular transformation possible in planar molecules of high symmetry will not hold in general; more elaborate analysis is required in nonplanar molecules, as already exemplified by the static JT images observed in the case of C_{60}^-.[24,25] Finally, beyond the information contained in images, JT-active systems are subject to peculiar dynamics, such as vibronic switching, JT-blockade,[51] and conductance bistability.[52]

■ AUTHOR INFORMATION

Corresponding Author
*E-mail: aapkaria@uci.edu.

Notes
The authors declare no competing financial interest.

■ ACKNOWLEDGMENTS

■ REFERENCES

(1) Chen, C. J. *Introduction to Scanning Tunneling Microscopy*; Oxford University Press: New York, 1993.

(2) Repp, J.; Meyer, G. Molecules on Insulating Films: Scanning-Tunneling Microscopy Imaging of Individual Molecular Orbitals. *Phys. Rev. Lett.* **2005**, *94*, 026803.

(3) Villagomez, C. J.; Zambelli, T.; Gauthier, S.; Gourdon, A.; Stojkovic, S.; Joachim, C. STM Images of a Large Organic Molecule Adsorbed on a Bare Metal Substrate or on a Thin Insulating Layer: Visualization of HOMO and LUMO. *Surf. Sci.* **2009**, *603*, 1526−1532.

(4) Gross, L.; Moll, N.; Mohn, F.; Curioni, A.; Meyer, G.; Hanke, F.; Persson, M. High-Resolution Molecular Orbital Imaging Using a p-Wave STM Tip. *Phys. Rev. Lett.* **2011**, *107*, 086101.

(5) Tersoff, J.; Hamann, D. R. Theory of the Scanning Tunneling Microscope. *Phys. Rev. B* **1985**, *31*, 805−813.

(6) Sautet, P. Images of Adsorbates with the Scanning Tunneling Microscope: Theoretical Approaches to the Contrast Mechanism. *Chem. Rev.* **1997**, *97*, 1097−1116.

(7) Kadish, K. M.; Smith, K. M.; Guilard, R. *Handbook of Porphyrin Science*; Academic Press: New York, 2003.

(8) Deisenhofer, J.; Norris, J. R. *The Photosynthetic Reaction Center*; Academic Press: New York, 1993.

(9) Jurow, M.; Schuckman, A. E.; Batteas, J. D.; Drain, C. M. Porphyrins as Molecular Electronic Components of Functional Devices. *Coord. Chem. Rev.* **2010**, *254*, 2297−2310.

(10) An, Y.-P.; Yang, Z.; Ratner, M. A. High-Efficiency Switching Effect in Porphyrin-Ethyne-Benzene Conjugates. *J. Chem. Phys.* **2011**, *135*, 044706.

(11) Gouterman, M. Study of the Effects of Substitution on the Absorption Spectra of Porphine. *J. Chem. Phys.* **1959**, *30*, 1139−1161.

(12) Gouterman, M. *The Porphyrins*; Dolphin, D., Ed.; Academic Press: New York, 1979; Vol. *III*, pp 1−166.

(13) Perrin, M. H.; Gouterman, M.; Perrin, C. L. Vibronic Coupling. VI. Vibronic Borrowing in Cyclic Polyenes and Porphyrin. *J. Chem. Phys.* **1969**, *50*, 4137−4150.

(14) Bersuker, I. B. *The Jahn-Teller Effect*; Cambridge University Press: Cambridge, U.K., 2006.

(15) Hu, S.; Lin, C.; Blackwood, M. E.; Mukherjee, A.; Spiro, T. G. Resonance Raman Structural Characterization of β-Substituted Metalloporphyrin π-Anion Radicals: Nature of the Jahn-Teller Effect. *J. Phys. Chem.* **1995**, *99*, 9694−9701.

(16) Seth, J.; Bocian, D. F. Electron Paramagnetic Resonance Studies of Metalloporphyrin Anion Radicals. Effects of Solvent, Counterion, Temperature, and Isotopic Substitution on the Jahn-Teller Active. *J. Am. Chem. Soc.* **1994**, *116*, 143−153.

(17) Hoffman, B. M.; Ratner, M. A. Jahn-Teller Effects in Metalloporphyrins and Other Four-Fold Symmetric Systems. *Mol. Phys.* **1978**, *35*, 901−925.

(18) Bersuker, I. B.; Stavrov, S. S. Structure and Properties of Metalloporphyrins and Hemoproteins: the Vibronic Approach. *Coord. Chem. Rev.* **1988**, *88*, 1−68.

(19) Jahn, H. A.; Teller, E. Stability of Polyatomic Molecules in Degenerate Electronic States. I. Orbital Degeneracy. *Proc. R. Soc. London Ser. A* **1937**, *161*, 220−235.

(20) Longuet-Higgins, H.; Opik, U. Studies of the Jahn-Teller Effect. II. The Dynamical Problem. *Proc. R. Soc. London Ser. A* **1958**, *244*, 1−16.

(21) Yarkony, D. R. Conical Intersections: The New Conventional Wisdom. *J. Phys. Chem. A* **2001**, *105*, 6277−6293.

(22) Berry, M. V. Quantal Phase Factors Accompanying Adiabatic Changes. *Proc. R. Soc. London Ser. A* **1984**, *392*, 45−57.

(23) Domcke, W.; Yarkony, D. R. Role of Conical Intersections in Molecular Spectroscopy and Photoinduced Chemical Dynamics. *Annu. Rev. Phys. Chem.* **2012**, *63*, 325.

(24) Wachowiak, A.; Yamachika, R.; Khoo, K. H.; Wang, Y.; Grobis, M.; Lee, D.-H.; Louie, S. G.; Crommie, M. F. Visualization of the Molecular Jahn-Teller Effect in an Insulating K_4C_{60} Monolayer. *Science* **2005**, *310*, 468−470.

(25) Hands, I. D.; Dunn, J. L.; Bates, C. A. Visualization of Static Jahn-Teller Effects in the Fullerene Anion C_{60}^-. *Phys. Rev. B* **2010**, *82*, 155425.

(26) Jaeger, R. M.; Kuhlenbeck, H.; Freund, H.-J.; Wuttig, M.; Hoffmann, W.; Franchy, R.; Ibach, H. Formation of a Well-Ordered Aluminium Oxide Overlayer by Oxidation of NiAl(110). *Surf. Sci.* **1991**, *259*, 235−252.

(27) Kresse, G.; Schmid, M.; Napetschnig, E.; Shishkin, M.; Kohler, L.; Varga, P. Structure of the Ultrathin Aluminum Oxide Film on NiAl(110). *Science* **2005**, *308*, 1440−1442.

(28) The NiAl-supported aluminium oxide film was modeled with a six-layer-thick slab where, the four undermost layers are of NiAl and the two topmost layers are of aluminum oxide.

(29) Klimes, J.; Bowler, D. R.; Michaelides, A. Chemical Accuracy for the van der Waals Density Functional. *J. Phys.: Condens. Matter* **2010**, *22*, 022201.

(30) Qiu, X. H.; Nazin, G. V.; Ho, W. Mechanisms of Reversible Conformational Transitions in a Single Molecule. *Phys. Rev. Lett.* **2004**, *93*, 196806.

(31) Wu, S. W.; Ogawa, N.; Nazin, G. V.; Ho, W. Conductance Hysteresis and Switching in a Single-Molecule Junction. *J. Phys. Chem. C* **2008**, *112*, 5241−5244.

(32) Simon, G. H.; König, T.; Nilius, M.; Rust, H.-P.; Heyde, M.; Freund, H.-J. Atomically Resolved Force Microscopy Images of Complex Surface Unit Cells: Ultrathin Alumina Film on NiAl(110). *Phys. Rev. B* **2008**, *78*, 113401.

(33) Libuda, J.; Winkelmann, F.; Bäumer, M.; Freund, H.-J.; Bertrams, Th.; Neddermeyer, H.; Müller, K. Structure and Defects of an Ordered Alumina Film on NiAl(110). *Surf. Sci.* **1994**, *318*, 61−73.

(34) Yoshizawa, K.; Nakayama, T.; Kamachi, T.; Kozlowski, P. M. Vibronic Interaction in Metalloporphyrin π-Anion Radicals. *J. Phys. Chem. A* **2007**, *111*, 852−857.

(35) McNaughten, R. L.; Roemelt, M.; Chin, J. M.; Schrock, R. R.; Neese, F.; Hoffman, B. M. Experimental and Theoretical EPR Study of Jahn-Teller-Active [HIPTN$_3$N]MoL Complexes (L = N$_2$, CO, NH$_3$). *J. Am. Chem. Soc.* **2010**, *132*, 8645−8656.

(36) Mulliken, R. S.; Rieke, C. A.; Brown, W. G. Hyperconjugation. *J. Am. Chem. Soc.* **1941**, *63*, 41−56.

(37) Ake, R. L.; Gouterman, M. Porphyrins XIV. Theory for the Luminescent State in VO, Co, Cu Complexes. *Theor. Chim. Acta* **1969**, *15*, 20−42.

(38) Hougen, J. T. Vibronic Interactions in Molecules with a Fourfold Symmetry Axis. *J. Mol. Spectrosc.* **1964**, *13*, 149−167.

(39) Ballhausen, C. J. Jahn-Teller Configurational Instability in Square-Planar Complexes. *Theor. Chim. Acta* **1965**, *3*, 368−374.

(40) Herzberg, G. Electronic Spectra of Polyatomic Molecules; Van Nostrand Reinhold: NewYork, 1966.

(41) In the analytic transformations, $\rho(\varphi) = \rho(\vartheta(\varphi))\partial\vartheta/\partial\varphi$, the explicit relation between angles and their derivatives must be included. In the case of ellipticity (7), this leads to distortions within quadrants. The consideration does not arise in numerical mappings of the polar graphs, where this is taken into account.

(42) Diaconu, C. V.; Batista, E. R.; Martin, R. L.; Smith, D. L.; Crone, B. K.; Crooker, S. A.; Smith's, D. L. Circularly Polarized Photo-luminescence from Platinum Porphyrins in Organic Hosts: Magnetic Field and Temperature Dependence. *J. Appl. Phys.* **2011**, *109*, 073513.

(43) Olsson, F. E.; Paavilainen, S.; Persson, M.; Repp, J.; Meyer, G. Multiple Charge States of Ag Atoms on Ultrathin NaCl Films. *Phys. Rev. Lett.* **2007**, *98*, 176803.

(44) Aharonov, Y.; Bohm, D. Significance of Electromagnetic Potentials in the Quantum Theory. *Phys. Rev.* **1959**, *115*, 485−491.

(45) Aharonov, Y.; Anandan, J. Phase Change During a Cyclic Quantum Evolution. *Phys. Rev. Lett.* **1987**, *58*, 1593−1596.

(46) Qiu, X. H.; Nazin, G. V.; Ho, W. Vibronic States in Single Molecule Electron Transport. *Phys. Rev. Lett.* **2004**, *92*, 206102.

(47) Li, Z.; Borguet, E. Determining Charge Transport Pathways Through Single Porphyrin Molecules Using Scanning Tunneling Microscopy Break Junctions. *J. Am. Chem. Soc.* **2012**, *134*, 63−66.

(48) Auwärter, W.; Seufert, K.; Bischoff, F.; Ecija, D.; Vijayaraghavan, S.; Joshi, S.; Klappenberger, F.; Samudrala, N.; Barth, J. V. A Surface-Anchored Molecular Four-Level Conductance Switch Based on Single Proton Transfer. *Nat. Nanotechnol.* **2012**, *7*, 41−46.

(49) Lee, H. J.; Lee, J. H.; Ho, W. Vibronic Transitions in Single Metalloporphyrins. *ChemPhysChem* **2005**, *6*, 971−975.

(50) Yan, S.; Ding, Z.; Xie, N.; Gong, H.; Sun, Q.; Guo, Y.; Shan, X.; Meng, S.; Lu, X. Turning On and Off the Rotational Oscillation of a Single Porphine Molecule by Molecular Charge State. *ACS Nano* **2012**, *6*, 4132−4136.

(51) Schultz, M. G.; Nunner, T. S.; Oppen, F. V. Berry-Phase Effects in Transport through Single Jahn-Teller Molecules. *Phys. Rev. B* **2008**, *77*, 075323.

(52) Maddox, J. B.; Harbola, U.; Mayoral, K.; Mukamel, S. Conductance Bistability in a Single Porphyrin Molecule in a STM

Junction: A Many-Body Simulation Study. *J. Phys. Chem. C* **2007**, *111*, 9516−9521.

J

dx.doi.org/10.1021/jp311894n | *J. Phys. Chem. A* XXXX, XXX, XXX−XXX